

QUANTUM-COUPLED SINGLE-ELECTRON THERMAL TO ELECTRIC CONVERSION SCHEME

D. M. Wu¹, P. L. Hagelstein¹, P. Chen², K. P. Sinha³, and A. Meulenber⁴

¹ Research Laboratory of Electronics, MIT, Cambridge, MA

² Harvard University, Cambridge, MA

³ Physics Department, IISc, Bangalore 560012, India

⁴ HiPi Consulting, Frederick, MD

ABSTRACT

Thermal to electric energy conversion with thermophotovoltaics relies on radiation emitted by a hot body, which limits the power per unit area to that of a blackbody. Microgap thermophotovoltaics take advantage of evanescent waves to obtain higher throughput, with the power per unit area limited by the internal blackbody, which is n^2 higher. We propose that even higher power per unit area can be achieved by taking advantage of thermal fluctuations in the near-surface electric fields. For this, we require a converter that couples to dipoles on the hot side, transferring excitation to promote carriers on the cold side which can be used to drive an electrical load. We analyze the simplest implementation of the scheme, in which excitation transfer occurs between matched quantum dots. Next, we examine thermal to electric conversion with a lossy dielectric (aluminum oxide) hot-side surface layer. We show that the throughput power per unit active area can exceed the n^2 blackbody limit with this kind of converter. With the use of small quantum dots, the scheme becomes very efficient theoretically, but will require advances in technology to fabricate.

I. INTRODUCTION

Thermal to electric energy conversion can be accomplished with high efficiency relative to the Carnot limit using thermophotovoltaics, but there is a fundamental limit on the power per unit area that can be converted [1, 2]. In such a device, the far-field radiation emitted from the hot side cannot exceed the relevant blackbody limit, which limits such converters to on the order of a watt/cm² converted power. In spite of this, there has been much interest in recent years in the development of thermophotovoltaic converters, and studies have been published indicating that the limitation on power per unit area does not preclude them from being competitive economically [3, 4]. Advances that would increase the converted power per unit area would lead directly to more favorable commercial prospects for the technology, which is a primary motivation for the research discussed in this work.

An important advance was made by DiMatteo and coworkers with the demonstration that the vacuum blackbody limit could be exceeded in a microgap thermophotovoltaic [5, 6]. The contribution of evanescent waves, negligible in a conventional thermophotovoltaic, becomes dominant in a microgap thermophotovoltaic, greatly increasing the throughput power per unit area. The blackbody limit in the microgap scheme approaches the internal blackbody limit inside the dielectrics, which is increased by a factor of n^2 over the vacuum case, where n is the index of refraction. The experimental results are consistent with this point of view, and a significant increase in throughput power was demonstrated. Microgap thermophotovoltaics for commercial applications are currently under development at MTPV LLC.

At this point, an obvious question presents itself: Is it possible to increase the throughput power beyond the n^2 blackbody limit associated with microgap thermophotovoltaics? By all rights the answer should be no, since we would not expect to be able to make more photons than allowed by statistical mechanics. Nevertheless, one can find in the literature a reason to be hopeful. For example, Greffet and coworkers have demonstrated that the thermal fluctuations of the electromagnetic field very near a hot surface can be very large, greatly exceeding the energy density of the blackbody for the temperature of the surface [7]. Since these thermal fluctuations include contributions from nonpropagating fields, the associated energy density can exceed the blackbody limit with no inconsistencies (since the blackbody limit is restricted to propagating fields).

To take advantage of this near-surface thermal fluctuation energy, a converter would be required. Since these fields do not propagate, they would not reach the interior of a photodiode. Hence, we would not expect a conventional photodiode to be able to convert this energy to electricity. Without

a fundamentally different kind of converter, the thermal energy associated with the near-surface thermal fluctuations remains tantalizingly out of reach.

We became interested in this problem, having been challenged by DiMatteo in 2002 to find a way to violate the n^2 blackbody limit. The answer at that time was seemingly clear: Since the n^2 blackbody limit comes about from transporting real photons, then to exceed it one needs to couple energy without relying on the photons. Instead, it was proposed to use direct coupling between dipoles on the hot side, and those on the cold side. At close range, dipole-dipole interactions are dominated by Coulomb coupling; further away, transverse photon exchange becomes important. That energy exchange can occur via Coulombic coupling is well known; in biophysics, such excitation transfer is termed the Förster effect [8, 9]. This effect is not included in the calculations of Greffet and coworkers since they use the Rytov formulation [10], which allows for the computation of thermal fluctuations for transverse fields (using the fluctuation-dissipation theorem) but not for Coulomb fields.

As noted above, we require a converter that is capable of scavenging power from both thermal Coulombic fluctuations and electromagnetic fluctuations near the surface. We recognize that there are a variety of different approaches to the problem; however, we have focused our attention on a quantum dot converter implementation on the cold side, and both quantum dot and lossy dielectric hot side structures. There are a number of reasons for this. On the one hand, the computations increase dramatically in complexity with the participation of more states; hence, a quantum dot implementation restricts the number of states involved, and is easier to calculate. On the other hand, the converter is more efficient when loss is minimized; hence, a quantum dot implementation has the potential to achieve higher efficiency than other implementations since the upper state lifetime can be longer. Since Coulomb fields dominate at short range, we have restricted our focus in this work to Coulomb interactions (the inclusion of transverse fields would greatly complicate the analysis, and we would expect only a modest increase in throughput power due to shallow angle waves in the gap).

The modeling that we report in this paper indicates that the throughput power per unit area can be very high, and that the theoretical efficiency can be close to the Carnot limit. Based on these results, it would seem that the approach is very promising. Unfortunately, to minimize the number of available states in the quantum dots, the quantum dots in the implementation under discussion must be very small. We have also relied on tunneling in order to transfer carriers between quantum dots and to contacts. Although impressive advances in quantum dot technology have occurred in recent years, the devices under consideration in this work probably cannot yet be fabricated to be

consistent with the requirements assumed in the modeling. Hence, the importance of the present work is that it sheds light on the approach in its ideal limit. Further advances in fabrication technology will occur, so that in the future for such devices we might expect the situation to change. Alternatively, one can envision different implementations which trade off performance to be more closely matched to current fabrication technologies, and which might be available sooner for experimentation.

II. QUANTUM-COUPLED CONVERTER

The basic device is perhaps best understood first in terms of a schematic, which we show in Figure 1. In this figure, we see a narrow vacuum gap that separates the hot-side structure (on the left) from the cold-side structure (on the right). We would like for excitation originating on the hot side to be transferred to the cold side, and ultimately turned into electrical work.

We begin by focusing on the two-level systems closest to the gap on either side. It is simplest conceptually to imagine matched quantum dots on the hot side and on the cold side, forgetting for a moment about the other parts of the structure. On the hot side, we would expect a carrier in the quantum dot to be in the excited state occasionally as a result of the elevated temperature, while on the cold side we would expect the carrier in the quantum dot to be in the ground state most of the time. The Coulomb interaction between the two carriers leads to a coupling with states in which the excitation of the two carriers is reversed. This is the excitation transfer step in which the energy available as carrier excitation energy on the hot side is transferred to the cold side, leading to the promotion of a carrier to the excited state. The associated coupling strength falls rapidly with gap separation, so that it is important only when the surfaces are close together on the nano scale. We would expect from energy conservation that the excitation transfer step will work best when the energy difference on the hot side is matched to the energy difference on the cold side.

Once the carrier on the cold side has been promoted, then we need to get it to the reservoir to the right (which is at elevated voltage) before it loses energy or transfers its excitation back. To do this, we arrange for the carrier to tunnel to a matched state in the second well. This state can be thought of as serving as an energy filter, which helps to restrict carriers from the high potential reservoir going back the ground state of the first well. Once the carrier reaches this state, then it can tunnel to the reservoir (contact or wire). Since it is at an elevated potential, electrical work can be done on a load, where another carrier arrives at the lower reservoir (ground), and the lower

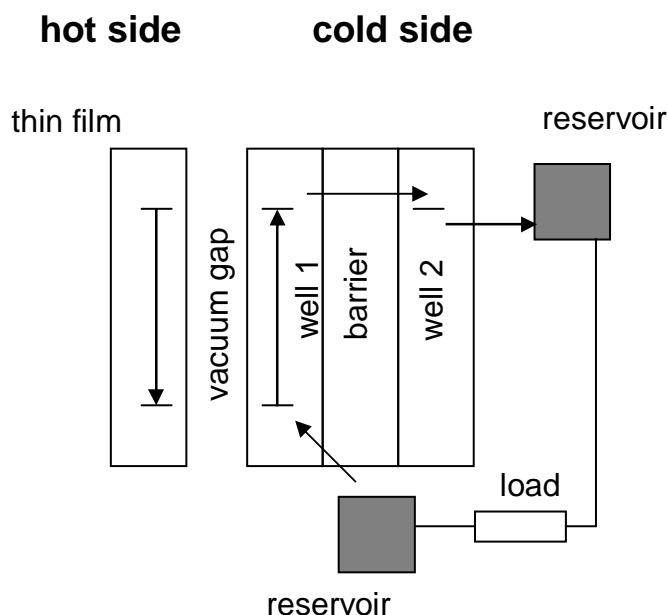


Figure 1: Schematic of the basic device showing the primary cold-side electron flow. Conceptually, dipoles on either side of a nanoscale gap are coupled through the Coulomb interaction, allowing for excitation transfer from the hot side to the cold side. The promoted carrier on the cold side tunnels through another state on the way to a contact, where the associated current is used to drive an electric load.

state of the first well is re-supplied.

In a sense, the cold-side structure is a single carrier engine that takes energy from the hot side and uses it to send carriers (one at a time) around an electrical circuit to do work. Note that during this process it is the excitation energy that is transferred from the hot-side to the cold-side, with no charge transport across the vacuum gap. The energy can only be extracted from the hot side when the cold side is very close, so that this converter is well matched to the functionality needed which was discussed above. It is a near-surface converter that accomplishes the conversion of energy from thermal Coulomb (and also electromagnetic) fluctuation energy available near the hot surface.

We might have included an additional energy filter state between the lower (ground) reservoir

and the two-state quantum dot on the cold side, which could help to isolate the upper level from the reservoir. Including such a state would further complicate an analysis that is already pretty complicated, without changing the results very much. As a practical matter, it would seem to be a reasonable idea to add a second filter state in a physical implementation.

III. MODELING

The development of a model for this kind of a device is interesting since the device operation requires both quantum coherence and loss. After first pursuing other approaches, we used a secular equations partitioning method similar to that described by Löwdin [11, 12], but augmented with loss [13]. We ultimately obtained good results with this model, which is based on: a Golden Rule calculation for an effective interaction between an initial continuum state and final continuum state; an integration over possible initial states as well as final state configurations; and an augmentation of the Hamiltonian with anti-Hermitian loss terms for modeling incoherent decays of intermediate states. Here, we summarize aspects of the model, and relegate details to the Appendices.

A. State definitions

The relevant single-electron states are illustrated in Figure 2. One sees that there are five discrete energy levels in the problem: levels a and b on the hot side; and levels 1, 2, and 3 on the cold side. In addition, one sees five different sets of continuum states associated with the five different reservoirs: reservoirs R_a and R_b on the hot side (with associated continuum states denoted by r_a and r_b); and reservoirs R_1 , R_2 , and R_3 on the cold side (with associated states denoted by r_1 , r_2 and r_3).

The excitation transfer process discussed briefly above leads to a correlation of the two particles, so that an appropriate quantum mechanical description of the overall system must be based on two-particle states. Because the specific example used in our modeling involved electrons, electrons will be used in the text, but the scheme can be implemented equally well using either electrons or holes. Note that this scheme involves intersubband transitions of single carriers, and not recombination of electron-hole pairs. It is convenient to adopt a bra and ket notation for the two-electron states such as $|r_a, 2\rangle$. The 24 possible combinations of such states are listed in Table I.

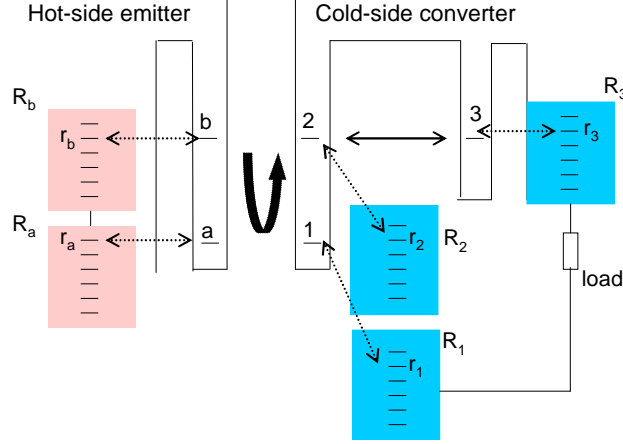


Figure 2: One electron state definitions used in the model.

TABLE I. List of possible two-electron states. The two-electron states are product states consisting of a hot-side one-electron state and a cold-side one-electron state.

HOT SIDE	COLD SIDE	POSSIBLE STATES
discrete	discrete	$ a, 1\rangle, b, 1\rangle, a, 2\rangle, b, 2\rangle, a, 3\rangle,$ and $ b, 3\rangle$
discrete	continuum	$ a, r_1\rangle, b, r_1\rangle, a, r_2\rangle, b, r_2\rangle, a, r_3\rangle,$ and $ b, r_3\rangle$
continuum	discrete	$ r_a, 1\rangle, r_b, 1\rangle, r_a, 2\rangle, r_b, 2\rangle, r_a, 3\rangle,$ and $ r_b, 3\rangle$
continuum	continuum	$ r_a, r_1\rangle, r_b, r_1\rangle, r_a, r_2\rangle, r_b, r_2\rangle, r_a, r_3\rangle,$ and $ r_b, r_3\rangle$

B. Model Hamiltonian

To analyze the device dynamics, we have made use of a model Hamiltonian appropriate to the two-electron states. The simplest such Hamiltonian is one in which states are coupled with interaction terms that are relevant to the problem. For example, consider the coupled-channel equation for a two-electron state $|b, 1\rangle$ which contains an excited electron on the hot side, and a ground state electron on the cold side:

$$E|b, 1\rangle = (E_b + E_1)|b, 1\rangle + U|a, 2\rangle + W_b|r_b, 1\rangle + W_1|b, r_1\rangle \quad (1)$$

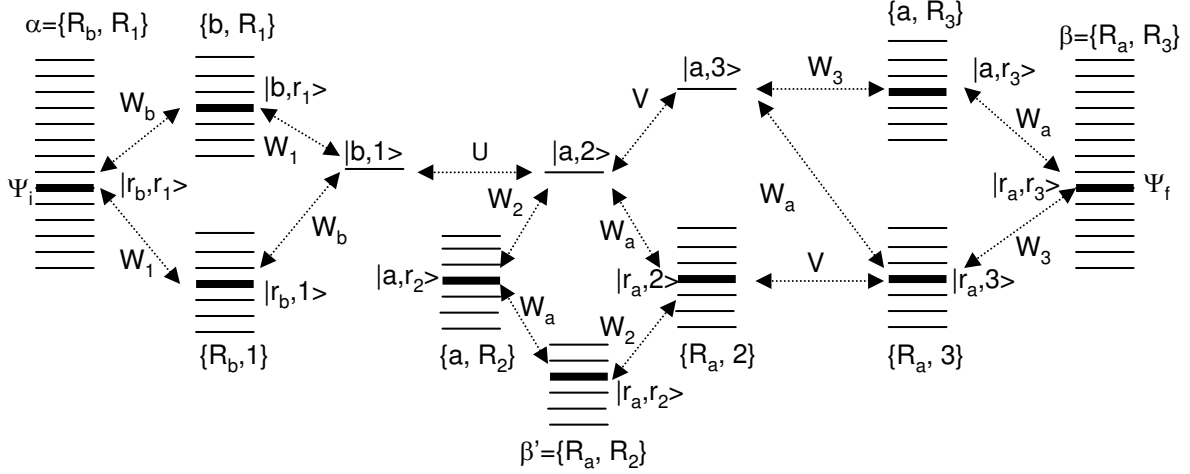


Figure 3: Two-electron levels and coupling used in the model. Three states are discrete: $|b, 1\rangle$, $|a, 2\rangle$ and $|a, 3\rangle$. There are three other discrete states listed in Table I but we do not include mechanisms that would couple to them in the model. The other two-electron states are continuum states, indicated here by sets of states.

The diagonal term is simply the combination of the two one-electron energies E_b and E_1 . The Coulomb interaction between the two electrons produces a dipole-dipole coupling which lowers the hot-side electron and raises the cold-side electron; the associated interaction strength for this coupling is U . There are in addition loss terms that couple the discrete states to continuum states; these are parameterized by W_b and W_1 . All of the coupled-channel equations together combine to form a very large eigenvalue problem, since there are two-electron basis states involving one-electron continuum states on both the hot side and the cold side. The couplings that we have included in the model under discussion are illustrated in Figure 3; the associated model Hamiltonian is given in Appendix A.

C. Transition rate

We compute the transition rate using the Golden Rule based on an effective interaction for a transition from an initial continuum state (with electrons in the R_b and R_1 reservoirs) to a final continuum state (with electrons in the R_a and R_3 reservoirs). We begin by selecting initial one-electron reservoir states r_b and r_1 to make an initial two-electron state $|r_b, r_1\rangle$, with a total energy $E = \epsilon_b + \epsilon_1$ (where ϵ_b is the energy of reservoir state r_b and ϵ_1 is the energy of reservoir state r_1). The final state is taken to be $|r_a, r_3\rangle$, with the same total energy $E = \epsilon_a + \epsilon_3$ (where ϵ_a is the energy for reservoir state r_a , and ϵ_3 is the energy for the reservoir state r_3). The transition rate between these two states is

$$\gamma(E) = \frac{2\pi}{\hbar} |\langle r_a, r_3 | U_{eff}(E) | r_b, r_1 \rangle|^2 \rho(E) \quad (2)$$

The effective interaction $U_{eff}(E)$ is obtained by eliminating algebraically all other basis states in the eigenvalue equation (which is possible since the energy is fixed). This is discussed further in Appendix A.

D. Integration over initial states

The current which flows from the reservoirs R_b and R_1 can be calculated by integrating the transition rate over all initial states. In these integrations, we need to weigh the states by their occupation probability (assuming thermal equilibrium within the reservoirs). Similarly, we also need to weigh the final states by the (thermodynamic) probability that they are not occupied. Taking these issues into account, we write for the current

$$\begin{aligned} I = & -e \int d\epsilon_b \int d\epsilon_1 \int d\epsilon_a \int d\epsilon_3 \rho_b(\epsilon_b) \rho_1(\epsilon_1) \rho_a(\epsilon_a) \rho_3(\epsilon_3) \\ & \frac{2\pi}{\hbar} |\langle r_a, r_3 | U_{eff}(\epsilon_1 + \epsilon_b) | r_b, r_1 \rangle|^2 \delta(\epsilon_b + \epsilon_1 - \epsilon_a - \epsilon_3) \\ & \left\{ p_b(\epsilon_b) p_1(\epsilon_1) [1 - p_a(\epsilon_a)] [1 - p_3(\epsilon_3)] - p_a(\epsilon_a) p_3(\epsilon_3) [1 - p_b(\epsilon_b)] [1 - p_1(\epsilon_1)] \right\} \end{aligned} \quad (3)$$

This equation includes contributions both from the forward direction (starting from $|r_b, r_1\rangle$), and from the return direction (starting from $|r_a, r_3\rangle$). The integration are taken over the one-electron continuum states associated with the initial and final two-electron states. The associated one-

electron density of state functions are $\rho_b(\epsilon_b)$, $\rho_1(\epsilon_1)$, $\rho_a(\epsilon_a)$, and $\rho_3(\epsilon_3)$. The one-electron occupation probabilities are $p_b(\epsilon_b)$, $p_1(\epsilon_1)$, $p_a(\epsilon_a)$, and $p_3(\epsilon_3)$. These are given by

$$\begin{aligned} p_a(\epsilon_a) &= \frac{1}{1 + e^{(\epsilon_a - \mu_a)/kT_h}} & p_b(\epsilon_b) &= \frac{1}{1 + e^{(\epsilon_b - \mu_b)/kT_h}} \\ p_1(\epsilon_1) &= \frac{1}{1 + e^{(\epsilon_1 - \mu_1)/kT_c}} & p_3(\epsilon_3) &= \frac{1}{1 + e^{(\epsilon_3 - \mu_3)/kT_c}} \end{aligned} \quad (4)$$

In these formula, the different μ_j are the Fermi level associated with the reservoir R_j . The voltage drop on the load is

$$V_L = - \frac{\mu_3 - \mu_1}{e} \quad (5)$$

For given V_L the current is determined by Equation (3, and the load resistance R_L must be chosen such that Ohm's law is satisfied:

$$V_L = I \times R_L \quad (6)$$

E. Thermal power transferred from the hot side

The calculation of the thermal power P_{th} delivered from the hot side involves multiplying individual transition rates within the integral that makes up the current by the electron energy difference on the hot side. We obtain

$$\begin{aligned} P_{th} &= \int d\epsilon_b \int d\epsilon_1 \int d\epsilon_a \int d\epsilon_3 \rho_b(\epsilon_b) \rho_1(\epsilon_1) \rho_a(\epsilon_a) \rho_3(\epsilon_3) \\ &\quad \frac{2\pi}{\hbar} |\langle r_a, r_3 | U_{eff}(\epsilon_1 + \epsilon_b) | r_b, r_1 \rangle|^2 \delta(\epsilon_b + \epsilon_1 - \epsilon_a - \epsilon_3) (\epsilon_b - \epsilon_a) \\ &\quad \left\{ p_b(\epsilon_b) p_1(\epsilon_1) [1 - p_a(\epsilon_a)] [1 - p_3(\epsilon_3)] - p_a(\epsilon_a) p_3(\epsilon_3) [1 - p_b(\epsilon_b)] [1 - p_1(\epsilon_1)] \right\} \end{aligned} \quad (7)$$

F. Power delivered to the load

The power delivered to the load can be calculated directly from the product of the current and the voltage drop on the load. The voltage drop on the load is

$$V_L = -\frac{\mu_3 - \mu_1}{e} \quad (8)$$

Consequently, we obtain for the load power P_L

$$P_L = V_L \times I \quad (9)$$

G. Efficiency and the Carnot limit

The device efficiency is the ratio of the load power to the thermal power

$$\eta = \frac{P_L}{P_{th}} \quad (10)$$

The Carnot limit is obeyed using this formulation for each incremental contribution, as outlined in Appendix B.

IV. Example with quantum dots on both the hot side and cold side

One way to implement this single-electron conversion scheme is to use quantum dots for both the hot and cold sides. Such an implementation corresponds most closely to the model that we have described. However, because of atomic self diffusion at high temperature, one would not like to use quantum dots on the hot side as they would degrade rapidly. This issue is addressed in example later on where a thin film is used instead. Nevertheless, our computations will be for 600K (which could be sustained temporarily) so that we can compare with the hot-side lossy dielectric example that follows.

To arrive at the design outlined below, we started by working with the model described above in order to optimize it in terms of relative U , V and W parameters. Then we carried out detailed device modeling for the energy levels of the quantum dots on the cold side and hot side, using these calculations to determine a design consistent with the optimized model parameters [13]. We chose a quantum dot implementation based on InAs/GaAs technology since it has been well studied in recent years. We review issues relating to the device model in Appendix C.

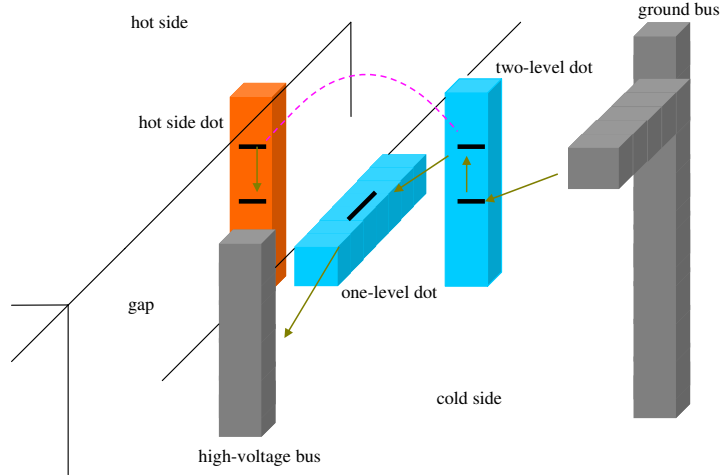


Figure 4: Proposed quantum dot implementation in three dimensions of the single-electron conversion scheme.

A. Proposed device

We show in Figure 4 three quantum dots implementing the state structure of the schematic in Figure 1. On the surface of the hot side is a single quantum dot (orange); on the surface of the cold side is the high-voltage bus (grey) and the two cold-side quantum dots (blue); below the surface is the ground bus (grey). The hot-side dot and the cold-side dot have matched level spacings and they face each other across the gap. The second cold-side dot (one-level dot) is positioned next to the first cold-side dot (two-level dot) to allow for tunneling. The ground bus provides an electron for the ground state of the two-level dot. This electron then gets promoted to an excited state via Coulombic energy transfer. The excited electron subsequently tunnels into the one-level dot before relaxing into the high-voltage bus to do work on the load. As noted earlier it is the excitation energy transfer across the gap that drives the cold-side carrier, and no charge moves from the hot-side to the cold-side.

There is a subtle feature of this design which should be noted. Since we have not separated the active two-state dot from the ground bus, one would expect coupling to both states of the active dot. This could degrade the device operation significantly because the upper state of the active dot could simply tunnel directly to the ground bus. A graded active quantum dot design in which the

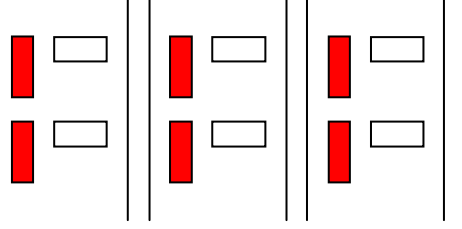


Figure 5: The cold-side surface as seen from above showing the area occupied by the quantum dots and the reservoirs of the different devices.

ground state is localized on one side of the dot (the one nearest the ground bus) while the excited state is localized on the other side (the one nearest the other cold-side quantum dot) could help alleviate this loss mechanism, though in this work the quantum dot is not graded for simplicity. An alternate approach would be to use an additional quantum dot with a single energy level matched to the lower state of the active dot to provide separation from the ground bus.

A single device can generate only a small amount of power, so that we assume that a great many such devices are patterned on the surface so as to provide significant power. An example of this patterning on the cold side is illustrated in Figure 5. The dots shown are tightly and precisely positioned which would present a fabrication challenge. We define active area to be the area of the cold-side active quantum dots (which accept the energy transfer from the hot side). In the results that follow, we focus on the power per unit active area, which is the transfer or load power of a single device divided by its active area.

B. Results

We consider the predicted device operation for a hot-side temperature of 600 K, and a cold-side temperature of 300 K. The load power per unit active area calculated from the model as a function of voltage assuming a matched load resistance is shown in Figure 6. The result is very nearly parabolic, which is typical of a linear thermoelectric or other linear thermal to electric converter. The maximum bias voltage at which thermal to electric conversion can occur (consistent with the Carnot limit) is

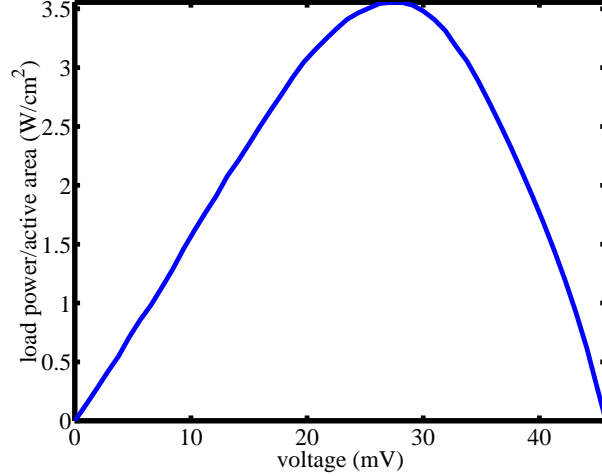


Figure 6: Load power per unit active area as a function of voltage for a 5 nm gap.

$$V_{max} = \frac{\Delta E}{q} \left(\frac{T_{hot} - T_{cold}}{T_{hot}} \right) \quad (11)$$

The transition energy that we used is 92 meV, so that the maximum voltage is 46 mV, consistent with this result. The maximum load power per unit active area is seen to be 3.5 W/cm², which is very good for the assumed hot side temperature.

We show the calculated efficiency as a function of voltage in Figure 7, along with the ideal efficiency $qV/\Delta E$. This ideal efficiency is the ratio of electrical work done by an electron at a voltage V divided by energy transferred from the hot side to promote the electron. Deviations from this ideal efficiency occurs primarily because the promoted electron is occasionally lost before making it to the reservoir. In this ideal limit, the maximum efficiency possible is the Carnot limit which occurs at V_{max} , at which the current goes to zero (so that no power is delivered to the load). There is a trade off for this device so that efficiency is sacrificed for load power. The maximum load power occurs at 27.5 mV, where the calculated efficiency is 26% (52% of the Carnot limit). The maximum efficiency occurs at 42 mV, where the calculated efficiency is 43% (86% of the Carnot limit).

The excitation transfer effect weakens considerably as the quantum wells are separated. The dipole-dipole matrix element arising from Coulomb interaction drops as $1/R^3$, and the load power is proportional to the square of this matrix element, so that we would expect the load power to

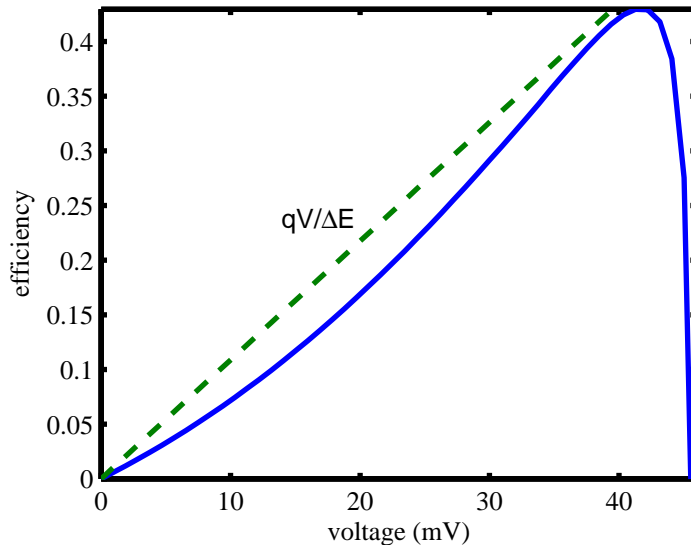


Figure 7: Efficiency as a function of voltage for a 5 nm gap.

follow a $1/R^6$ scaling law asymptotically. When the gap separation is on the order of the dipole moment, the scaling is more gentle. In Figure 8 we show the maximum load power per unit active area as a function of gap thickness, which shows a steep drop as the gap separation increases, but weaker than the $1/R^6$ asymptotic dependence below 10 nm (the maximum load power drops from 39 W/cm² at 1 nm to 521 mW/cm² at 10 nm). The dashed line indicates $1/R^6$ dependence while the horizontal solid line is the blackbody limit at 600 K and the dash-dot line is the n^2 blackbody limit.

V. Example with a dielectric on the hot side

In the example of the previous section, we focused on an implementation where thermal to electric conversion is mediated by Coulomb coupling between quantum dots on the hot side and on the cold side, which corresponds most closely to the model presented above. Choosing a small quantum dot as we have done allows for a reduction in the loss of the excited state of the active dot, and results in a very high calculated efficiency. However, the construction of a converter with

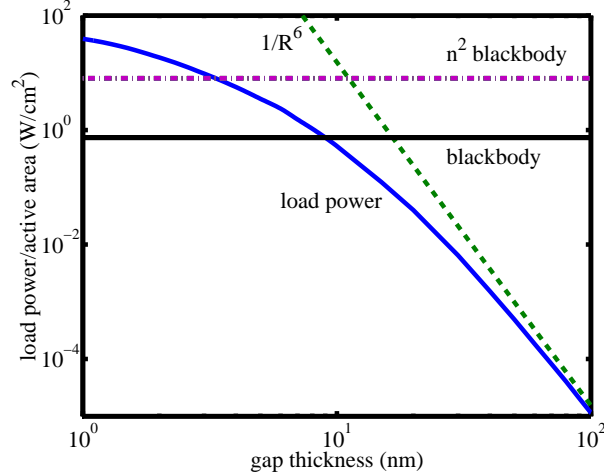


Figure 8: Maximum load power per unit active area as a function of gap thickness. The dashed line indicates $1/R^6$ dependence. The horizontal solid line is the blackbody limit at 600 K and the dash-dot line is the n^2 blackbody limit.

a large number of such small quantum dots is not easy. Nevertheless, the converted power per unit active area is very high, as was hoped for.

The alignment of small quantum dots as seems to be required in this example is technically challenging. In addition, one would like to avoid the use of quantum dots on the hot side because of atomic diffusion. These issues are addressed in a second example which we consider in this section. In this example, we replace the hot-side quantum dots with a uniform lossy dielectric, focusing on the coupling between the dipole of the quantum dot on the cold side, and the many constituent dipoles in the hot-side material.

A. Design and modeling issues

The most informative example given the discussion above would be to adopt the same cold-side structure, and simply replace the quantum dots on the hot side with a lossy dielectric. To do so, we require a lossy dielectric that can interact strongly near the resonance (92 meV) of the active quantum dot. Of the materials for which optical constants in the infrared are readily available, we found that Al_2O_3 has the highest absorption coefficient, so we choose Al_2O_3 for our hot-side

material. Note that loss can have a large effect on the rate of excitation transfer [14], but we have not included this effect in the modeling reported here.

Next, we need to think about how the model described above might be adapted for this device. For the hot-side quantum dot case, the load power is maximized when the excitation transfer and tunneling are coherent processes with similar matrix elements. However, the lossy dielectric is made up of a great many dipoles, each with a much weaker interaction individually, with contributions that add incoherently. In principle, we can apply our model to describe thermal to electric conversion due to the coupling to each dipole individually. When we carry out such a computation, we find that the model leads to a simpler expression (this is in the limit of a weak hot-side dipole with a fast relaxation time) which we are able to sum systematically over all similar dipoles. This computation is outlined in Appendix E.

The room temperature optical constants for aluminum oxide are obtained from [15]. The absorption coefficient for the temperature of 600 K is inferred from the room temperature values through Equation (67) of Appendix E. There appears to be two sets of inconsistent data from [16] and [17], and we have chosen to use the data from [16]. We have used the data for the ordinary polarization because it has one plane of polarization as opposed to the extraordinary polarization which is only in one direction; therefore, we expect the data for the ordinary polarization to play a dominant role.

B. Results

In Figure 9 we show the load power per unit active area as a function of voltage with a 5 nm gap. Once again the shape is roughly parabolic, with increased nonlinearity as compared with our previous example. This time however the load power per unit active area is much larger, reaching a maximum of 328 W/cm². It would be reasonable to ask why the load power has increased so much, since all that has been done is to modify the hot side material between the two examples. The answer is simply that the contribution of a large number of weak dipoles overwhelms the contribution from a single very strong dipole.

The calculated efficiency as a function of voltage is shown in Figure 10; the maximum efficiency is 37% (74% of the Carnot limit) at 39 mV. Once again the efficiency is not far from the ideal limit ($qV/\Delta E$), and we see that the result is similar to what we found in the previous example. This can be interpreted simply as noting that the cold-side converter works pretty much the same independent of what hot-side source that thermal power is being drawn from. The minor reduction

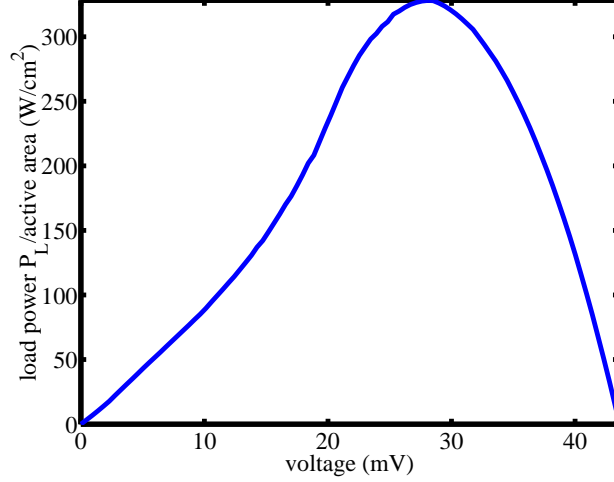


Figure 9: Load power per unit active area as a function of voltage with a modified aluminum oxide hot side for a 5 nm gap.

in efficiency which is apparent between the two examples is attributable primarily to the increase in the bandwidth of the thermal power transferred from the hot side.

The calculated maximum load power per unit active area as a function of gap separation is shown in Figure 11. One observes a rapid drop off with increasing separation (the maximum load power drops from 2900 W/cm² at 1 nm to 89 mW/cm² at 100 nm); however, this drop off is much less dramatic than in our previous example.

The reason for this is that the cold-side dipole couples to a large number of dipoles at different distances, so that increasing the gap does not have as large an effect for the large number of more distant dipoles. The asymptotic dependence is $1/L^3$ (where L is the gap thickness), which can be understood simply from integrating the underlying $1/R^6$ dependence of the square of the Coulomb interaction matrix element over the hot-side volume

$$2\pi \int_0^\infty dz \int_0^\infty \rho d\rho \frac{1}{[(z+L)^2 + \rho^2]^3} = \frac{2\pi}{L^3} \int_0^\infty dt \int_0^\infty x dx \frac{1}{[(t+1)^2 + x^2]^3} = \frac{\pi}{6L^3} \quad (12)$$

This dependence is observed in our calculations when the gap separation is much larger than the cold-side dipole moment.

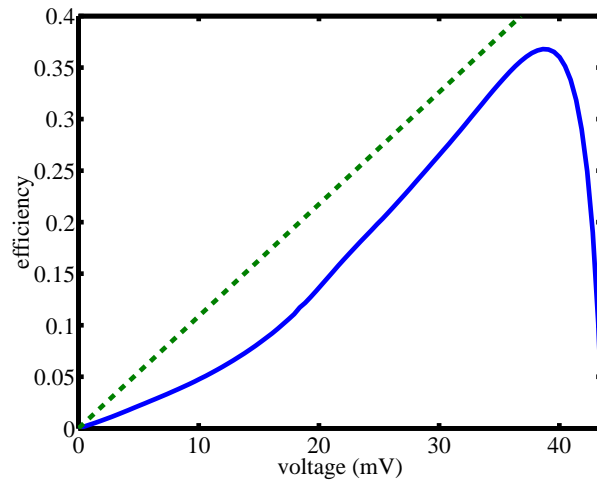


Figure 10: Efficiency as a function of voltage with a modified aluminum oxide hot side for a 5 nm gap.

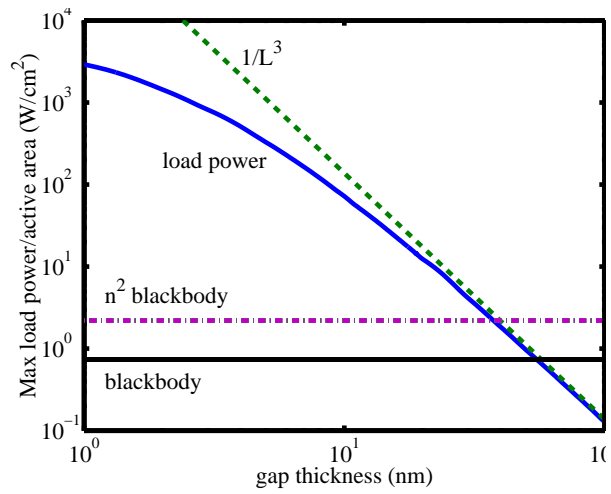


Figure 11: Maximum load power per unit active area with a modified aluminum oxide hot side as a function of gap thickness. The dashed line indicates $1/L^3$ dependence. The horizontal solid line is the blackbody limit at 600 K and the dash-dot line is the n^2 blackbody limit.

VI. Summary and discussion

As mentioned above, we were motivated by DiMatteo’s challenge to see whether it was possible to improve over the n^2 blackbody limit of microgap thermophotovoltaics. DiMatteo’s intuition at the time was that there should be a way to take advantage of direct coupling between the electrons on either side of a very small gap. We note a recent work by some of the authors has addressed this problem in a different way, by making use of the available electromagnetic energy very close to the surface [18]. Our response was focus on direct coupling between electrons on the hot side and cold side using a near-surface thermal to electric converter, so as to avoid relying on the conversion of the thermal energy to photons. At close range the dipole-dipole interaction is dominated by the Coulomb interaction, so that we proposed to transfer the thermal energy to our converter directly using Coulomb coupling. A consequence of this is that any converter which works in this way must be very close (on the nano scale) to the hot surface.

In this work, the technical issues associated with developing a suitable mathematical model for excitation transfer of the thermal power and the subsequent conversion have dominated the device design. The scheme depends critically on quantum coherence effects, loss, and thermodynamics; all of which must be treated appropriately in order to obtain a reliable description of device performance. Because of this, a relatively large number of two-particle states are required at the outset for a proper treatment, and this provided motivation for us to consider physical systems with the fewest number of accessible states in an implementation. Hence, the simplest mathematical description of the scheme comes about from a quantum dot implementation on both the cold and hot side, which leads to designs which probably cannot be built yet given the current state of quantum dot technology.

Nevertheless, we felt that it was important to work through a design iteration, to try to better understand the scheme, the design issues, and perhaps more importantly to understand how best to move forward to modified versions of the scheme which are more accessible. One such modification was discussed in Section V, where the hot-side quantum dot was replaced with a uniform lossy dielectric (which removes the headaches of quantum dot relative alignment on the two sides, and degradation of the hot-side dot by atomic diffusion).

The devices discussed in this work achieve a very high maximum load power per unit active area, which perhaps can best be seen by considering the load power per unit active area in the case of a uniform aluminum oxide hot side, shown in Figure 9. The maximum load power per unit active area is computed to be 323 W/cm^2 . The full spectrum vacuum blackbody limit at 600 K

is 0.73 W/cm^2 , while the n^2 internal blackbody limit is higher by an order of magnitude. This demonstrates that the approach is capable of achieving a transferred thermal power per unit active area (which is even larger) well in excess of the n^2 blackbody limit for the materials used.

However, there remains the issue of fabrication. Given the rapid developments being reported constantly in the area of nano technology, we may need simply to wait a few years before devices similar to that described in this work can be built. On the other hand, it is clear that we should be able to design other devices capable of converting near surface thermal Coulomb fluctuations. What has made this design so challenging is the decision to maximize the upper state lifetime on the cold side, which maximizes the device efficiency. In larger quantum dots, quantum wires, and in quantum wells, the upper state lifetime is shortened considerably. For example, the measured upper state lifetime could be tens of picoseconds for quantum dots as compared to picosecond range reported in two-dimensional semiconductors [25]. Under such conditions, it is still possible to scavenge surface Coulomb fluctuations, but at a possibly lower conversion efficiency. We can envision implementing well 1 and well 2 in Figure 1 using quantum wires or quantum wells, the analysis of which remains as future work.

ACKNOWLEDGMENTS

The authors gratefully acknowledge the financial support of Draper Laboratory, MTPV Corporation, and MTPV LLC.

APPENDIX A: SECULAR EQUATIONS PARTITIONING METHOD

In this Appendix we outline the partitioning technique to eliminate intermediate states that we used to obtain an effective interaction $U_{eff}(E)$ including loss which is used in Section III. This type of calculation has been carried out for the effective couplings between the donor and acceptor states in aggregated molecular assemblies [19] (although the calculation in [19] does not include loss). Our model can also be thought of as a special case of a more general basic problem. Suppose that there are two reservoirs connected through arbitrary levels and we want to calculate the flux between the two reservoirs. Specifically, we want to compute the flux from an initial state Ψ_i to a final state Ψ_f . Then the relevant indirect interaction can be obtained by eliminating the Ψ_j 's from all of the intermediate states.

To include loss, we make use of sectors. The basic idea starts with the argument that a proper Hamiltonian is Hermitian, and hence lossless. But we are interested in developing a simple model Hamiltonian that includes a description of loss. The simplest way to accomplish this is to start with a lossless problem, and then to divide the associated state space into different sectors. We then focus on one sector, in which case transitions to states outside of this sector appear as loss terms in the sector Hamiltonian. This approach can be used systematically to develop model sector Hamiltonians which contain antihermitian elements, in the context of a full Hamiltonian which is Hermitian.

Basic sector equations

We begin with coupled-channel equations for the different states of interest, starting from the initial state Ψ_i , going to the final state Ψ_f , which is coupled indirectly through intermediate states Ψ_j :

$$E \Psi_i = H_i \Psi_i + \sum_{j \neq i, f} V_{ij} \Psi_j \quad (13)$$

$$E \Psi_j = H_j \Psi_j + \sum_{j' \neq i, j, f} V_{jj'} \Psi_{j'} + V_{ji} \Psi_i + V_{jf} \Psi_f \quad (14)$$

$$E \Psi_f = H_f \Psi_f + \sum_{j \neq i, f} V_{fj} \Psi_j \quad (15)$$

The situation corresponds to the coupling indicated in Figure 12.

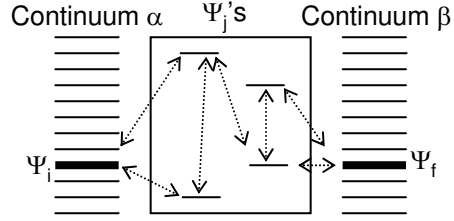


Figure 12: Energy level diagram of basic problem. Initial state Ψ_i resides in continuum α while the final state Ψ_f resides in continuum β . They are connected through a network of intermediate states Ψ_j 's.

The intermediate levels described by the different Ψ_j can couple to (and decay to) states outside of the sector of interest, which is accounted for by the introduction of loss terms. Hence, in general we will write model sector Hamiltonian terms in Equation (14) as

$$H_j = E_j - i \frac{\hbar \Gamma_j}{2} \quad (16)$$

where E_j is the energy of level j , and where the imaginary part accounts for loss.

Loss term

The sector method is well adapted to problems involving loss, and has been widely used in the past. Here, we review briefly an example in which Golden Rule decay is obtained using the sector method. In this example we assume that level Ψ_1 in the sector of interest is coupled to a continuum of states Ψ_j in another sector, with matrix elements W_j (see Figure 13).

The associated sector equations are

$$E \Psi_1 = E_1 \Psi_1 + \sum_{j \neq 1} W_j \Psi_j \quad (17)$$

$$E \Psi_j = E_j \Psi_j + W_j \Psi_1 \quad (18)$$

Substituting Eq. (18) into Eq. (17) gives

$$E \Psi_1 = E_1 \Psi_1 + \sum_{j \neq 1} \frac{|W_j|^2 \Psi_1}{E - E_j}$$

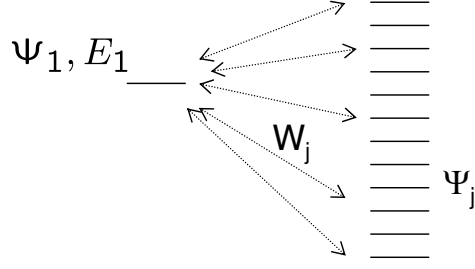


Figure 13: Lossy level Ψ_1 coupled to a continuum of states Ψ_j 's with matrix elements W_j 's

We evaluate the second term in the above equation:

$$\sum_{j \neq 1} \frac{W_j}{E - E_j} \approx - \int \frac{|W_j|^2 \rho(E_j)}{E_j - E} dE_j = - \oint_{C_1} \frac{|W_j|^2 \rho(E_j)}{E_j - E} dE_j - \oint_{C_2} \frac{|W_j|^2 \rho(E_j)}{E_j - E} dE_j$$

where contour C_1 consists of two line paths $E_j = -\infty \sim E - \epsilon$ and $E_j = E + \epsilon \sim \infty$, and contour C_2 is a hemisphere $E_j = E + \epsilon \cdot e^{i\theta}$, $\theta = -\pi \sim 0$. In the limit $\epsilon \rightarrow 0^+$, the two contour integrals become:

$$- \oint_{C_1} \frac{|W_j|^2 \rho(E_j)}{E_j - E} dE_j \longrightarrow \sum_{E_j \neq E} \frac{|W_j|^2}{E_j - E}$$

which is the self-energy term, and

$$- \oint_{C_2} \frac{|W_j|^2 \rho(E_j)}{E_j - E} dE_j \longrightarrow -i\pi |W_j|^2 \rho(E_j) = -i \frac{\hbar\Gamma}{2}$$

which is the loss term, and Γ here is the Golden Rule decay rate of level Ψ_1 [21].

Vector and matrix notation

We introduce some matrix notations to facilitate our discussion.

1. $\bar{\Psi}_j$ is the column vector of all Ψ_j 's.
2. \bar{K} is the coupling matrix among the Ψ_j 's:

$$\forall p, q \neq i, f \quad (\bar{K})_{pq} = H_p \delta_{pq} + V_{pq} \quad (19)$$

Because V_{pq} is assumed real,

$$V_{pq} = V_{qp}$$

Therefore $\overline{\overline{K}}$ is symmetric.

3. \overline{V}^i is the coupling column vector between Ψ_i and Ψ_j 's:

$$\left(\overline{V}^i\right)_j = V_{ij} \quad (20)$$

4. \overline{V}^f is the coupling column vector between Ψ_f and Ψ_j 's:

$$\left(\overline{V}^f\right)_j = V_{fj} \quad (21)$$

Effective potential using vectors and matrices

With the above definitions, we rewrite the algebraic sector equations into matrix equations:

$$E \Psi_i = H_i \Psi_i + \left(\overline{V}^i\right)^T \overline{\Psi}_j \quad (22)$$

$$E \overline{\Psi}_j = \overline{\overline{K}} \overline{\Psi}_j + \overline{V}^i \Psi_i + \overline{V}^f \Psi_f \quad (23)$$

$$E \Psi_f = H_f \Psi_f + \left(\overline{V}^f\right)^T \overline{\Psi}_j \quad (24)$$

From eq. (23),

$$\overline{\Psi}_j = \left[E - \overline{\overline{K}}\right]^{-1} \cdot \left[\overline{V}^i \Psi_i + \overline{V}^f \Psi_f\right] \quad (25)$$

Substituting eq. (25) into eq. (22), we obtain

$$E \Psi_i = H_i \Psi_i + U_{ii} \Psi_i + U_{if} \Psi_f \quad (26)$$

where

$$U_{ii} \equiv \left(\overline{V}^i\right)^T \cdot \left[E - \overline{\overline{K}}\right]^{-1} \overline{V}^i \quad (27)$$

$$U_{if} \equiv (\bar{V}^i)^T \cdot [E - \bar{K}]^{-1} \bar{V}^f \quad (28)$$

Substituting eq. (25) into eq. (24), we obtain

$$E \Psi_f = H_f \Psi_f + U_{ff} \Psi_f + U_{fi} \Psi_i \quad (29)$$

where

$$U_{ff} \equiv (\bar{V}^f)^T \cdot [E - \bar{K}]^{-1} \cdot \bar{V}^f \quad (30)$$

$$U_{fi} \equiv (\bar{V}^f)^T \cdot [E - \bar{K}]^{-1} \cdot \bar{V}^i \quad (31)$$

U_{fi} is equal to U_{if} :

$$\begin{aligned} U_{if} &= U_{if}^T = \left[(\bar{V}^i)^T \cdot [E - \bar{K}]^{-1} \cdot \bar{V}^f \right]^T \\ &= \left[[E - \bar{K}]^{-1} \cdot \bar{V}^f \right]^T \cdot \bar{V}^i = (\bar{V}^f)^T \cdot [E - \bar{K}]^{-1} \cdot \bar{V}^i = U_{fi} \end{aligned}$$

Note that U_{if} is equal to its transpose because U_{if} is a scalar.

Model Hamiltonian

For the basic device with quantum dots on both the cold side and hot side, we can develop a model sector Hamiltonian (\bar{K}) which implements excitation transfer through Coulomb coupling, tunneling, as well as loss. Let us define the real and imaginary parts of \bar{K} :

$$\bar{K} \equiv \bar{A} - i \hbar \frac{\bar{\Gamma}}{2}. \quad (32)$$

where \bar{A} contains the real components of \bar{K} , namely the energy terms, and $\bar{\Gamma}$ contains the imaginary components of \bar{K} , namely the loss terms. The columns and rows of the matrices are listed with the following order of intermediate states: $|b, r_1\rangle$, $|r_b, 1\rangle$, $|b, 1\rangle$, $|a, r_2\rangle$, $|a, 2\rangle$, $|a, 3\rangle$, $|r_a, 2\rangle$, $|a, r_3\rangle$, and $|r_a, 3\rangle$. The sector Hamiltonian which implements the model that we used, and which is illustrated in Figure 3 is

$$\bar{A} \equiv \begin{bmatrix} E_b + \epsilon_1 & 0 & W_1 & 0 & 0 & 0 & 0 & 0 & 0 \\ 0 & \epsilon_b + E_1 & W_b & 0 & 0 & 0 & 0 & 0 & 0 \\ W_1 & W_b & E_b + E_1 & 0 & U & 0 & 0 & 0 & 0 \\ 0 & 0 & 0 & E_a + \epsilon_2 & W_2 & 0 & 0 & 0 & 0 \\ 0 & 0 & U & W_2 & E_a + E_2 & V & W_a & 0 & 0 \\ 0 & 0 & 0 & 0 & V & E_a + E_3 & 0 & W_3 & W_a \\ 0 & 0 & 0 & 0 & W_a & 0 & \epsilon_a + E_2 & 0 & V \\ 0 & 0 & 0 & 0 & 0 & W_3 & 0 & E_a + \epsilon_3 & 0 \\ 0 & 0 & 0 & 0 & 0 & W_a & V & 0 & \epsilon_a + E_3 \end{bmatrix} \quad (33)$$

$$\bar{\Gamma} \equiv \begin{bmatrix} \Gamma_{b,r_1} & 0 & 0 & 0 & 0 & 0 & 0 & 0 & 0 \\ 0 & \Gamma_{r_b,1} & 0 & 0 & 0 & 0 & 0 & 0 & 0 \\ 0 & 0 & \Gamma_{b,1} & 0 & 0 & 0 & 0 & 0 & 0 \\ 0 & 0 & 0 & \Gamma_{a,r_2} & 0 & 0 & 0 & 0 & 0 \\ 0 & 0 & 0 & 0 & \Gamma_{a,2} & 0 & 0 & 0 & 0 \\ 0 & 0 & 0 & 0 & 0 & \Gamma_{a,3} & 0 & 0 & 0 \\ 0 & 0 & 0 & 0 & 0 & 0 & \Gamma_{r_a,2} & 0 & 0 \\ 0 & 0 & 0 & 0 & 0 & 0 & 0 & \Gamma_{a,r_3} & 0 \\ 0 & 0 & 0 & 0 & 0 & 0 & 0 & 0 & \Gamma_{r_a,3} \end{bmatrix} \quad (34)$$

The energy of the system is

$$E = \epsilon_b + \epsilon_1 = \epsilon_a + \epsilon_3.$$

The Γ 's are obtained from the Golden Rule:

$$\Gamma_{b,r_1} = \frac{2\pi}{\hbar} W_b^2 \rho_b(\epsilon_b) \quad (35)$$

$$\Gamma_{r_b,1} = \frac{2\pi}{\hbar} W_1^2 \rho_1(\epsilon_1) \quad (36)$$

$$\Gamma_{b,1} = \frac{2\pi}{\hbar} W_b^2 \rho_b(E - E_1) + \frac{2\pi}{\hbar} W_1^2 \rho_1(E - E_b) \quad (37)$$

$$\Gamma_{a,r_2} = \frac{2\pi}{\hbar} W_a^2 \rho_a(\epsilon_a) \quad (38)$$

$$\Gamma_{a,2} = \frac{2\pi}{\hbar} W_a^2 \rho_a(E - E_2) + \frac{2\pi}{\hbar} W_2^2 \rho_2(E - E_a) \quad (39)$$

$$\Gamma_{a,3} = \frac{2\pi}{\hbar} W_a^2 \rho_a(E - E_3) + \frac{2\pi}{\hbar} W_3^2 \rho_3(E - E_a) \quad (40)$$

$$\Gamma_{r_a,2} = \frac{2\pi}{\hbar} W_2^2 \rho_2(\epsilon_2) \quad (41)$$

$$\Gamma_{a,r_3} = \frac{2\pi}{\hbar} W_a^2 \rho_a(\epsilon_a) \quad (42)$$

$$\Gamma_{r_a,3} = \frac{2\pi}{\hbar} W_3^2 \rho_3(\epsilon_3) \quad (43)$$

Effective interaction between initial and final state

The coupling column vectors for the initial and final states are

$$\bar{V}^i = \left[W_b \quad W_1 \quad 0 \quad 0 \quad 0 \quad 0 \quad 0 \quad 0 \quad 0 \quad 0 \right]^T \quad (44)$$

and

$$\bar{V}^f = \left[0 \quad 0 \quad 0 \quad 0 \quad 0 \quad 0 \quad 0 \quad 0 \quad W_a \quad W_3 \right]^T \quad (45)$$

These are appropriate, since we first must populate level b on the hot side, and level 1 on the cold side, prior to the excitation transfer process, and the process is deemed to be completed in an irreversible sense when the hot-side electron in state a returns to its reservoir, and the electron in state 3 goes to the contact. The effective matrix element between the initial state and the final state is then

$$U_{eff} = U_{fi} = \left(\bar{V}^f \right)^T \cdot \left[E - \bar{K} \right]^{-1} \cdot \bar{V}^i. \quad (46)$$

APPENDIX B: CARNOT LIMIT

The individual forward and reverse current paths in the model are in detailed balance, so that one would expect that the efficiency would be constrained by the Carnot limit. We have found this to be so in our calculations. One can also derive this from the basic model, by working with the occupation probabilities that appear in the integral that defines the current [Equation (3)]. The term in brackets that contain the occupation probabilities can be written in the form

$$\left\{ p_b(\epsilon_b)p_1(\epsilon_1)[1 - p_a(\epsilon_a)][1 - p_3(\epsilon_3)] - p_a(\epsilon_a)p_3(\epsilon_3)[1 - p_b(\epsilon_b)][1 - p_1(\epsilon_1)] \right\} = \frac{e^{\frac{\epsilon_a - \mu_a}{kT_h}} e^{\frac{\epsilon_3 - \mu_3}{kT_c}} - e^{\frac{\epsilon_b - \mu_b}{kT_h}} e^{\frac{\epsilon_1 - \mu_1}{kT_c}}}{\left(1 + e^{\frac{\epsilon_b - \mu_b}{kT_h}}\right) \left(1 + e^{\frac{\epsilon_1 - \mu_1}{kT_c}}\right) \left(1 + e^{\frac{\epsilon_a - \mu_a}{kT_h}}\right) \left(1 + e^{\frac{\epsilon_3 - \mu_3}{kT_c}}\right)} \quad (47)$$

One sees that the electron flow is positive when the numerator is positive, which occurs when

$$\frac{\epsilon_a - \mu_a}{T_h} + \frac{\epsilon_3 - \mu_3}{T_c} \geq \frac{\epsilon_b - \mu_b}{T_h} + \frac{\epsilon_1 - \mu_1}{T_c}$$

which reduces to

$$\mu_3 - \mu_1 < (\epsilon_b - \epsilon_a) \left(\frac{T_h - T_c}{T_h} \right) \quad (48)$$

remembering that $\epsilon_b - \epsilon_a = \epsilon_3 - \epsilon_1$ from energy conservation. Since the incremental power delivered to the load is proportional to $\mu_3 - \mu_1$, and the incremental thermal power is proportional to $\epsilon_b - \epsilon_a$, the incremental efficiency for each contribution is $(\mu_3 - \mu_1)/(\epsilon_b - \epsilon_a)$. If the incremental thermal power is positive, then either the electron flow is positive and the energy quanta transferred $\epsilon_b - \epsilon_a$ is positive; or else the electron flow is negative and the energy quanta transferred $\epsilon_b - \epsilon_a$ is negative. In both cases the incremental efficiency for each contribution satisfies the Carnot limit

$$\frac{\mu_3 - \mu_1}{\epsilon_b - \epsilon_a} < \frac{T_h - T_c}{T_h} \quad (49)$$

When this inequality is not satisfied, the incremental thermal power is either zero or negative, and the associated contribution does not improve device operation.

APPENDIX C: DESIGN AND PARAMETERS FOR THE DOT-DOT EXAMPLE

Much effort was devoted in this study to understand how to optimize this kind of thermal to electric converter [13]. Initially this optimization was done with simpler models, and it quickly became clear that essentially everything was determined by the magnitude of the Coulomb coupling matrix element which mediates excitation transfer. For a gap of 5 nm, the Coulomb coupling matrix element U is 2.5×10^{-4} eV. Once the coupling matrix element is known, then the tunneling rate from state 2 to state 3 must be matched to it (as was determined by a large number of model computations aimed at optimizing the system). Finally, the cold-side relaxation times to the reservoirs need to be matched to twice the associated Rabi frequencies. In what follows we review the design of a proposed device which was designed in this way. We have focused on InAs/GaAs in this design since it is one of the most extensively studied quantum dot systems.

Materials and dimensions

Dot 1 has $x \times y \times z$ dimension $(145 \text{ \AA}) \times (45 \text{ \AA}) \times (45 \text{ \AA})$ and is implemented using InAs. The energy separation of the dot 1 levels is 0.092 eV. Both reservoir 1 and reservoir 2 are made up of n-type InAs with $6 \times 10^{18} \text{ cm}^{-3}$ doping. The hot-side is made up of InAs quantum dots on GaAs matrix, with the dots of the same size as the cold-side dot 1 and aligned such that they face each other across the gap. There is a layer of n-typed $2.1 \times 10^{18} \text{ cm}^{-3}$ doped InAs 65 \AA below the hot-side dots. On the cold-side, dot 2 is assumed to be InAs, with dimensions $(45 \text{ \AA}) \times (45 \text{ \AA}) \times (70 \text{ \AA})$, and is horizontally pointing to the top part of dot 1. Dot 2 holds a level that is lower than the excited level of dot 1 by 40 meV such that at a voltage of 40 mV they become resonant. Note that Figure 4 is not drawn to scale. The distance between dot 1 and dot 2 is 35 \AA . Reservoir 1 branch is horizontally positioned 35 \AA away from the center of dot 1. Due to this spatial orientation, reservoir 1 coupling to the excited level of dot 1 is small. Reservoir 2 is located 35 \AA next to dot 2. The substrate on the cold-side is GaAs. The gap thickness is assumed to be nanometer-scaled. Gaps of 5-15 nm are well within the present state of the art [22] and a nanometer gap has been used to demonstrate cooling by room-temperature thermionic emission [23].

Quantum dot parameters

A calculation of the energy levels in InAs/GaAs quantum dots is performed in [24] and we use

their conduction band discontinuity of 697 mV in this work. Unlike [24] which assumes a unique effective mass 0.067 throughout the structure, we use the InAs effective mass 0.024 in the InAs region and the GaAs effective mass of 0.067 in the GaAs region. The two levels in dot 1 are computed to be 525 meV and 617 meV above the conduction band edge of InAs. The level in dot 2 is computed to be 577 meV above the conduction band edge of InAs. We calculate the quantum dot wavefunctions to estimate the tunneling matrix element to be $V = 3.3$ meV, which matches a relaxation time of $\hbar/V = 0.2$ ps.

Fermi levels

The Fermi levels of the reservoirs are found from

$$N_D = N_c F_{1/2}(\eta_c)$$

where N_D is the doping level and N_c is the effective density of states of the conduction band of InAs $8.7 \times 10^{16} \text{ cm}^{-3}$. $F_{1/2}$ is the Fermi-Dirac integral of order 1/2. η_c is the normalized energy spacing between the Fermi level and the conduction band edge $\eta_c = (E_F - E_c)/kT$. Both the hot-side and the cold-side reservoirs are solved to have the Fermi level above the conduction band edge by 525 meV, matching the ground-state energy of dot 1 and the hot-side dot.

Relaxation times

The relaxation times on the hot-side dot levels is estimated using the approach described in [13]. For the hot-side dot, the ground state relaxation time is calculated to be 0.2 ps while that of the excited state is estimated to be 0.06 ps. On the cold-side, level 1 and level 3 also have a relaxation time of 0.2 ps. The relaxation of level 2 is considered below.

Loss

As noted before, the relaxation of level 2 in dot 1 constitutes loss. This relaxation consists of three components. The first component is the phonon-assisted relaxation. The second component is the relaxation into reservoir 1. The last component is the relaxation into surface states. The phonon-assisted [25] relaxation is characterized by a relaxation time of 37 ps from [25]. The level

spacing between the two levels in dot 1 is 92 meV, which is 20 meV detuning from 72 meV, a multiple of the GaAs LO-phonon energy $\hbar\omega_0=36$ meV. This detuning is the same as that in [25] and therefore we use their measured lifetime of 37 ps as the phonon-assisted loss relaxation time of the excited level in dot 1. This lifetime of QD levels is considerably longer than that of bulk or two-dimensional heterostructures because there are no levels to relax to at $\hbar\omega_0$ harmonics; namely, the density of states is restricted. In addition, the polaronic nature of the confined electron coupled to the phonon [25] results in inefficient phonon-assisted relaxation, and therefore implementing the cold-side with quantum dots has an advantage of lower loss compared to the two-dimensional heterostructure implementation.

The lifetimes for the relaxations into reservoir 1 and the surface are estimated using the approach described in [13]. The lifetime of level 2 relaxation into reservoir 1 is estimated to be 20 ps. The relaxation time into the surface states is dependent on how far the dot is from the surface and in principle can be made long. A discussion on the relaxation into surface states is given in [13]. Here we only consider the effects of the phonon-assisted relaxation of lifetime 37 ps and relaxation into reservoir 1 of lifetime 20 ps. The total equivalent relaxation time is

$$\left(\frac{1}{20 \text{ ps}} + \frac{1}{37 \text{ ps}}\right)^{-1} \approx 13 \text{ ps}$$

APPENDIX D: FABRICATION ISSUES

The fabrication of quantum dots presents a challenge. The quantum dots need to meet two criteria. First of all, the dots need to be small enough to contain only one or two states. One common method of quantum dot fabrication is the Stranski-Krastanow (SK) growth mode, namely strain-induced self-organization growth of quantum dots [26]. Using the SK growth, InAs/GaAs quantum dots containing as few as three states have been reported [25] (flat elliptical lens-shaped dots with height 2.5 nm and base length 25 nm) and it is conceivable that fewer-state dots are achievable. Second, precise positioning of the dots is required. Using pre-patterned templates with the SK method, growth of InAs/GaAs dots on designated areas has been carried out [27, 28, 29, 30], but exact positioning of single quantum dots is still difficult.

There are other nanofabrication techniques aside from the SK method. Electron beam lithography has been shown to produce resist dots of approximately 5 to 6 nm[31]. Scanning tunneling

microscope lithography has been used to fabricate 15 nm wide trenches in Si [32]. Dip-pen nanolithography has been used to write alkanethiols with 30-nanometer linewidth on a gold thin film [33] and to deposit AuC₁₂H₂₅S (2.5 nm in diameter) gold nanocluster islands (lateral dimensions 67 nm × 72 nm) on a silica surface. It is possible that these methods could be adapted to construct nano-structures demonstrating the quantum properties we desire.

Another fabrication issue is the highly ordered nano-sized reservoir array as shown in Figure 4 and Figure 5. The reservoir branch that couples to the cold-side dot requires smaller dimension and might be implemented as conductive carbon nanotubes. The size of single-well carbon nanotubes is typically 1 to 3 nm in diameter [34]. The reservoir interconnects could potentially be of larger sizes and might be implemented as doped regions or semiconductor nanowires. Doped regions can be shaped by resist of which resolution can be 5 to 6 nm with electron beam lithography [31]. Good control over the diameter and length of nanowires has been demonstrated in nearly monodisperse indium phosphide nanowires of diameters 10, 20, and 30 nm and lengths 2, 4, 6, and 9 μm [35]. Doping is required to make the nanowires into electron reservoirs and we have seen examples of B-doped silicon nanowires of diameter 150 nm and P-doped silicon nanowires of diameter 90 nm [36]. Connecting individual wires into the complex branched array structure of Figure 4 and Figure 5 presents a great challenge, which would require further research.

APPENDIX E: MODEL WITH A HOT-SIDE DIELECTRIC

Because of coherence, the full model Hamiltonian of Appendix A must be used to obtain good answers for devices with hot-side quantum dots. However, when we use a lossy dielectric on the hot side, the interaction of each individual hot-side dipole with the cold-side converter simplifies. In this case the effective interaction U_{eff} (between state $|b, r_1\rangle$ and state $|a, r_3\rangle$) simplifies to [13]

$$U_{\text{eff}} = \frac{UVW_1W_3}{d_{b,1}(d_{a,2}d_{a,3} - V^2) - U^2d_{a,3}} \quad (50)$$

where

$$d_{b,1} = \epsilon_1 - E_1 + i\hbar\Gamma_{b,1}/2 \quad \Gamma_{b,1} = \frac{2\pi}{\hbar}W_1^2\rho_1(\epsilon_1) \quad (51)$$

$$d_{a,2} = \hbar\omega + \epsilon_1 - E_2 + i\hbar\Gamma_{a,2}/2 \quad \Gamma_{a,2} = \frac{2\pi}{\hbar}W_2^2\rho_2(\hbar\omega + \epsilon_1) \quad (52)$$

$$d_{a,3} = \hbar\omega + \epsilon_1 - E_3 + i\hbar\Gamma_{a,3}/2 \quad \Gamma_{a,3} = \frac{2\pi}{\hbar}W_3^2\rho_3(\hbar\omega + \epsilon_1) \quad (53)$$

The notations are as follows: ϵ_1 is the reservoir state r_1 energy; E_1 , E_2 , and E_3 are the energies of the cold-side levels 1, 2, and 3; W_1 , W_2 , and W_3 are the coupling matrix elements between levels 1, 2, 3 and their associated reservoir levels; ρ_1 , ρ_2 , and ρ_3 are the reservoir density of states. The energy spacing between the two levels a and b of the hot-side dipole is $\hbar\omega$.

Current resulting from a single hot-side dipole

For the dot-dot design described previously, at a gap of 5 nm the Coulomb matrix element U between the hot-side and the cold-side quantum dot dipoles is calculated to be 2.5×10^{-4} eV, or $\hbar/U = 2.6$ ps, which is ten times longer than the cold-side relaxation rate. Even for a gap of 1 nm, the $\hbar/U = 0.76$ ps is still long. The hot-side dielectric dipoles are expected to be smaller than the transition dipole moment of an artificial quantum dot. In addition, most of the dipoles are distributed further away in the bulk of the hot-side. Hence the matrix element U between a single hot-side dielectric dipole and the cold-side quantum dot dipole is much smaller than the cold-side relaxation rates. In this case, we approximate the effective matrix element U_{eff} by omitting the U term in the denominator, and we obtain

$$\frac{U_{\text{eff}}}{U} \approx \frac{VW_1W_3}{d_{b,1}(d_{a,2}d_{a,3} - V^2)}. \quad (54)$$

The contribution from a single hot-side dipole of level a and level b with energy spacing $\hbar\omega$ to the device current is then

$$I_{\text{dipole}} = q|U|^2 \int d\epsilon_1 \rho_1(\epsilon_1) \rho_3(\epsilon_1 + \hbar\omega) \frac{2\pi}{\hbar} |\langle r_a, r_3 | \frac{U_{\text{eff}}}{U} | r_b, r_1 \rangle|^2 \\ \times \{p_{\text{high}}(\omega)p_1(\epsilon_1) [1 - p_3(\epsilon_1 + \hbar\omega)] - p_{\text{low}}(\omega)p_3(\epsilon_1 + \hbar\omega) [1 - p_1(\epsilon_1)]\} \quad (55)$$

where $p_{\text{low}}(\omega)$ is the thermal equilibrium probability that the dipole is in its lower energy state (level a) and $p_{\text{high}}(\omega)$ is the probability that the dipole is in the higher energy state (level b). The values of these two probabilities are

$$p_{\text{low}}(\omega) = \frac{1}{1 + e^{-\hbar\omega/kT_h}} \quad p_{\text{high}}(\omega) = \frac{e^{-\hbar\omega/kT_h}}{1 + e^{-\hbar\omega/kT_h}} \quad (56)$$

Coulomb interaction matrix element

To calculate the total device current, we integrate through all the dipoles with different frequencies and spatial positions. Because the dipoles in principle can have arbitrary orientation, we use the averaged Coulomb matrix element squared in the following expression. The dipole interaction energy between a hot-side dipole \mathbf{d}_j and a cold-side dipole \mathbf{d}_i is [37]

$$U = \frac{4\epsilon_0\epsilon_2|\mathbf{d}_j|}{(\epsilon_0 + \epsilon_1)(\epsilon_0 + \epsilon_2)} \sum_{n=0}^{\infty} \left(\frac{\epsilon_0 - \epsilon_1}{\epsilon_0 + \epsilon_1}\right)^n \left(\frac{\epsilon_0 - \epsilon_2}{\epsilon_0 + \epsilon_2}\right)^n \frac{1}{4\pi\epsilon_2|\Delta\mathbf{R}_{ijn}|^3} \left[\mathbf{d}_i \cdot \hat{\mathbf{n}}_j - 3(\mathbf{d}_i \cdot \hat{\mathbf{i}}_{ijn})(\hat{\mathbf{i}}_{ijn} \cdot \hat{\mathbf{n}}_j)\right] \quad (57)$$

where $\hat{\mathbf{n}}_j$ is the unit vector in the direction of \mathbf{d}_j , and $\hat{\mathbf{i}}_{ijn}$ is a unit vector in the direction of $\mathbf{d}_i - \mathbf{d}_j$.

The hot-side dipole in principle can have a random orientation, and we do an averaging to relate the expectation of the Coulomb matrix element squared to the dipole moment:

$$\begin{aligned} \langle |U|^2 \rangle &= \frac{\epsilon_0^2 |\mathbf{d}_j|^2}{\pi(\epsilon_0 + \epsilon_1)^2(\epsilon_0 + \epsilon_2)^2} \left\langle \left| \sum_{n=0}^{\infty} \left(\frac{\epsilon_0 - \epsilon_1}{\epsilon_0 + \epsilon_1}\right)^n \left(\frac{\epsilon_0 - \epsilon_2}{\epsilon_0 + \epsilon_2}\right)^n \frac{1}{|\Delta\mathbf{R}_{ijn}|^3} \left[\mathbf{d}_i - 3(\mathbf{d}_i \cdot \hat{\mathbf{i}}_{ijn})\hat{\mathbf{i}}_{ijn}\right] \cdot \hat{\mathbf{n}}_j \right|^2 \right\rangle \\ &= \frac{\epsilon_0^2 |\mathbf{d}_j|^2}{3\pi(\epsilon_0 + \epsilon_1)^2(\epsilon_0 + \epsilon_2)^2} \left| \sum_{n=0}^{\infty} \left(\frac{\epsilon_0 - \epsilon_1}{\epsilon_0 + \epsilon_1}\right)^n \left(\frac{\epsilon_0 - \epsilon_2}{\epsilon_0 + \epsilon_2}\right)^n \frac{1}{|\Delta\mathbf{R}_{ijn}|^3} \left[\mathbf{d}_i - 3(\mathbf{d}_i \cdot \hat{\mathbf{i}}_{ijn})\hat{\mathbf{i}}_{ijn}\right] \right|^2. \quad (58) \end{aligned}$$

Total current

The total current with contributions from all the dipoles is then

$$\begin{aligned}
I_{\text{total}} = & \frac{2\pi q}{\hbar} \int d^3\mathbf{r} \rho_r \int dE \rho_E(\hbar\omega) |\mathbf{d}_j|^2 f(\mathbf{r}, \omega) \int d\epsilon_1 \rho_1(\epsilon_1) \rho_3(\epsilon_1 + \hbar\omega) \\
& \times |\langle r_a, r_3 | \frac{U_{\text{eff}}}{U} | r_b, r_1 \rangle|^2 \{ p_{\text{high}}(\omega) p_1(\epsilon_1) [1 - p_3(\epsilon_1 + \hbar\omega)] \\
& \quad - p_{\text{low}}(\omega) p_3(\epsilon_1 + \hbar\omega) [1 - p_1(\epsilon_1)] \}
\end{aligned} \tag{59}$$

where ρ_r (assumed uniform) and ρ_ω are the spatial and spectral density of dipoles in the dielectric. We have defined $f(\mathbf{r}, \omega)$ as

$$f(\mathbf{r}, \omega) = \frac{\epsilon_0^2}{3\pi(\epsilon_0 + \epsilon_1)^2(\epsilon_0 + \epsilon_2)^2} \left| \sum_{n=0}^{\infty} \left(\frac{\epsilon_0 - \epsilon_1}{\epsilon_0 + \epsilon_2} \right)^n \left(\frac{\epsilon_0 - \epsilon_2}{\epsilon_0 + \epsilon_2} \right)^n \frac{1}{|\Delta\mathbf{R}_{ijn}|^3} \left[\mathbf{d}_i - 3(\mathbf{d}_i \cdot \hat{\mathbf{i}}_{ijn}) \hat{\mathbf{i}}_{ijn} \right] \right|^2 \tag{60}$$

Absorption coefficient

The expressions that we have obtained rely on orientation averages of the square of the dipole moments in the dielectric. The same terms arise in expressions for the optical constants, which are readily available for many materials. Hence, we would like to rewrite our expressions in terms of the optical absorption coefficient so that we can use published optical data to evaluate device performance.

The photoabsorption rate per unit volume is related to the dipole moment and the density of states through the Golden Rule [38]

$$\gamma = \frac{2\pi}{\hbar} |\mathbf{d}|^2 |\mathbf{E}_0|^2 \rho(E) \tag{61}$$

where γ is the absorption rate, \mathbf{d} is the dipole moment, \mathbf{E}_0 is the electric field of the light, and $\rho(E)$ is the density of dipoles per unit energy $E = \hbar\omega$. Expressing γ in terms of the absorption coefficient [38], we get

$$\gamma = \frac{\alpha S}{\hbar\omega} \tag{62}$$

The intensity can be computed from the expectation value of the Poynting vector operator

$$S = |\langle \hat{\mathbf{E}} \times \hat{\mathbf{H}} \rangle| \quad (63)$$

Applying the field operators quantized in a lossy medium [39]:

$$S = \sqrt{\frac{\epsilon_0}{\mu_0}} \langle (\mathbf{E}_0 + \mathbf{E}_0^*) (\mathbf{E}_0 \cdot (n + ik) + \mathbf{E}_0^* (n - ik)) \rangle = 4n \sqrt{\frac{\epsilon_0}{\mu_0}} \langle \text{Re}\{\mathbf{E}_0\}^2 \rangle = 2n \sqrt{\frac{\epsilon_0}{\mu_0}} |\mathbf{E}_0|^2 \quad (64)$$

where n is the real part of the refractive index. Combining equations (61), (62), and (64) gives the absorption coefficient

$$\alpha = \sqrt{\frac{\mu_0}{\epsilon_0}} \frac{\pi\omega}{n} |\mathbf{d}|^2 \rho(E) \quad (65)$$

Current in terms of the absorption coefficient

We can now recast the current relation in terms of the hot-side optical absorption coefficient. To this end, we note that the quantity $\rho(E)$ actually encompasses three components. The first component (ρ_r) is the spatial density of dipoles; the second ($\rho_E(\hbar\omega)$) is the density of states of the two-level dipoles with energy spacing $\hbar\omega$; the third (p_{low}) is the equilibrium probability that the dipole is in its lower energy state. Altogether, we have the following equation

$$\alpha(\omega) = \sqrt{\frac{\mu_0}{\epsilon_0}} \frac{\pi\omega}{n(\omega)} |\mathbf{d}|^2 p_{\text{low}} \rho_r \rho_E(\hbar\omega) = \frac{\pi\omega}{n(\omega)(1 + e^{-\hbar\omega/kT})} \sqrt{\frac{\mu_0}{\epsilon_0}} |\mathbf{d}|^2 \rho_r \rho_E(\hbar\omega) \quad (66)$$

Therefore we can express the integral involving the hot-side dipole moments, occupation probability, and density of states, as a function of the absorption coefficient:

$$|\mathbf{d}|^2 \rho_r p_{\text{low}}(\omega) \rho_E(\hbar\omega) = \sqrt{\frac{\epsilon_0}{\mu_0}} \frac{n\alpha(\omega)}{\pi\omega} \quad (67)$$

Similarly

$$|\mathbf{d}|^2 \rho_r p_{\text{high}}(\omega) \rho_E(\hbar\omega) = e^{-\hbar\omega/kT_h} \sqrt{\frac{\epsilon_0}{\mu_0}} \frac{n\alpha(\omega)}{\pi\omega} \quad (68)$$

From these results, we arrive at an expression for the current that can be evaluated given the refractive index and absorption coefficient data of the materials and the cold-side dipole moment $|\mathbf{d}_i|$:

$$\begin{aligned}
I_{\text{total}} = & \int dE \int d^3\mathbf{r} f(\mathbf{r}, \omega) \alpha(\omega) \frac{2qn(\omega)}{\hbar\omega} \sqrt{\frac{\epsilon_0}{\mu_0}} \int d\epsilon_1 |\langle r_a, r_3 | \frac{U_{\text{eff}}}{U} | r_b, r_1 \rangle|^2 \rho_1(\epsilon_1) \rho_3(\epsilon_1 + \hbar\omega) \\
& \times \{e^{-\hbar\omega/kT_h} p_1(\epsilon_1) [1 - p_3(\epsilon_1 + \hbar\omega)] - p_3(\epsilon_3 + \hbar\omega) [1 - p_1(\epsilon_1)]\} \tag{69}
\end{aligned}$$

We can evaluate the above expression to obtain the load current. Similar formulas can be derived for the transferred power and load power.

REFERENCES

1. D. Chubb, *Fundamentals of Thermophotovoltaic Energy Conversion*, Elsevier Science (2007).
2. M. G. Mauk, *Survey of Thermoelectric Devices*, Springer 637 (2006).
3. L. M. Fraas, J. E. Avery, and H. X. Huang, *Semicond. Sci. and Technol.* **18** S247 (2003).
4. G. Palfinger, B. Bitnar, W. Durisch, J.-C. Mayor, D. Grutzmacher, and J. Gobrecht, *AIP Conf. Proc.* **653** 29 (2003).
5. R. S. DiMatteo, P. Greiff, S. L. Finberg, K. A. Young-Waithe, H. K. H. Choy, M. M. Masaki, and C. G. Fonstad, *Appl. Phys. Lett.* **79**, 1894 (2001).
6. U.S. Patent #6,084,173 issued July 4, 2000
7. K. Joulain, J.-P. Mulet, F. Marquier, R. Carminati, J.-J. Greffet, *Surface Science Reports* **57** 59 (2005).
8. Th. Förster, *Discuss. Faraday Soc.* **27** 7 (1959).
9. *Resonance Energy Transfer*, edited by D. L. Andrews and A. A. Demidov, John Wiley and sons, New York (1999).
10. S. Rytov, Y. Kravstov, V. Tatarskii, *Principles of Statistical Radiophysics*, vol. 3, Springer-Verlag, Berlin (1989).
11. P. Lowdin, *J. Chem. Phys.* **19**, 1391 (1951).
12. P. Lowdin, *J. Mol. Spectrosc.* **10**, 12 (1963).
13. D. M. Wu, *Quantum-coupled single-electron thermal to electric conversion scheme*, MIT PhD Thesis, (2007).
14. P. L. Hagelstein and I. U. Chaudhary, *J. Phys. B* **41**, 135501 (2008).
15. E. D. Palik, *Handbook of Optical Constants of Solids III*, San Diego : Academic Press.
16. T. Tomiki, Y. Ganaga, T. Futemma, T. Shikenbaru, Y. Aiura, M. Yuri, S. Sato, H. Fututani, H. Kato, T. Miyahara, J. Tamashiro, and A. Yonesu, *J. Phys. Soc. Jpn.* **62**. 1372 (1993).

17. R. H. French, H. Mullejans, and D. J. Jones, *J. Am. Ceram. Soc.* **81**, 2549 (1998).
18. A. Meulenber and K. P. Sinha, "Spectral selectivity from resonant-coupling in microgap-TPV," to be published *JRSE* 2009.
19. G. D. Scholes, X. J. Jordanides, and G. R. Fleming, *J. Phys. Chem. B* **105**, 1640 (2001).
20. X. J. Jordanides, G. D. Scholes, and G. R. Fleming, *J. Phys. Chem. B* **105**, 1652 (2001).
21. P. L. Hagelstein, S. D. Senturia, and T. P. Orlando, *Introductory Applied Quantum and Statistical Mechanics*, Wiley-Interscience (2004).
22. Y. Hishinuma, T. H. Genalle, B. Y. Mozyzges, and T. W. Kenny, *Appl. Phys. Lett.* **78**, 2572 (2001)..
23. Y. Hishinuma, T. H. Genalle, B. Y. Mozyzges, and T. W. Kenny, *J. Appl. Phys.* **94**, 4690 (2003).
24. J.-Y. Marzin and G. Bastard, *Solid State Commun.* **92**, 437 (1994).
25. S. Sauvage, P. Boucaud, R.P.S.M. Lobo, F. Bras, G. Fishman, R. Prazeres, F. Glotin, J. M. Ortega, and J.-M. Gerard, *Phys. Rev. Lett.* **88**, 177402 (2002).
26. I. N. Stranski and V.. L. Krastanow, *kad. Wiss. Lit. Mainz Math.-Natur. Kl. Iib.* **146**, 797 (1937).
27. M. H. Baier, S. Watanabe, E. Pelucchi and E. Kapon, *Appl. Phys. Lett.* **84**, 1943 (2004).
28. J. H. Lee, Zh. M. Wang, B. L. Liang, K. A. Sablon, and N. W. Strom, *Semicond. sci. technol.* **21**, 1547 (2006).
29. R. Ohashi, T. Ohtsuka, N. Ohta, A. Yam, and M. Konagai, *Thin Solid Films* **464-465**, 237 (2004).
30. D. Schuh, J. Bauer, E. Uccelli, R. Schlz, A. Kress, F. Hofbauer, J.J. Finley, and G. Abstreiter, *Physica E* **26**, 72 (2005).
31. M. J. Lercel and H. G. Craighead, *Appl. Phys. Lett.* **68**, 1504 (1996).
32. F. K. Perkins, E. A. Dobisz, S. L. Brandow, J. M. Calvert, J. E. Kosakowski, and C. R. K. Marrian, *Appl. Phys. Lett.* **68**, 550 (1996).

33. R. D. Piner, J. Zhu, F. Xu, S. Hong and C. A. Mirkin, *Science* **283**, 661 (1999).
34. R. Saito, G. Dresselhaus, and M. S. Dresselhaus, *Physical Properties of Carbon Nanotubes*, Imperial College Press (1998).
35. M. K. Gudiksen, J. Wang, and C. M. Lieber, *J. Phys. Chem. B* **105**, 4062 (2001).
36. Y. Cui, X. Duan, J. Hu, and C. M. Lieber, *J. Phys. Chem. B* **104**, 5214 (2000).
37. P. L. Hagelstein, *Electrostatic potentials near a gap*, unpublished.
38. P. L. Hagelstein, *On the Intersubband Scheme with Coulomb Coupling*, unpublished.
39. R. Matloob and R. Loudon, *Phys. Rev. A* **52**, 4823 (1995).